CONDENSED
MATTER
PHYSICS

Review

Structure and properties of the films based on ternary transition metal borides: theory and experiment

A. A. Onoprienko (iD), V. I. Ivashchenko (iD), V. I. Shevchenko (iD) *

Frantsevich Institute for Problems of Materials Sciences, NAS of Ukraine, Kyiv, Ukraine

The review presents the results of theoretical and experimental studies of the structure, bonding between atoms, mechanical properties, thermal stability, and oxidation and corrosion resistance of films based on ternary transition metal borides.

Key words: *ternary transition metal borides, films, structure, properties*

1. Introduction

The increasing industrial demand for protective coatings with high hardness, good elastic properties and thermal stability calls for the investigation of new materials. Though transition metal nitrides and carbides are successfully used for different tasks in automotive or aerospace industries, the search for improved materials is an essential problem.

Boron is one of the hardest materials known. Therefore, a promising way to achieve strong materials with exceptional properties is the investigation of borides, in particular of transition metal (TM) borides. Transition metal borides showed potential applications as hard protective thin films and electrical contact materials. Among the stoichiometric variety of transition metal borides (TM-B, TM-B_2, TM-B_4, TM-B_{14}, etc.), the diborides exhibit useful properties such as high hardness and wear resistance, high melting points, high conductivity, chemical inertness, good corrosion resistance, and good thermal stability [1–15].

The binary TM-B_2 compounds are known to crystallize in two related hexagonal structures: α-AlB_2-prototype or ω-W_2B_{5-z}-prototype (figure 1) [16]. A large number of early TMB_2 compounds (such as TiB_2, ZrB_2, VB_2, etc.) have the AlB_2 structure type and crystallize in a three atoms unit cell with space group 191 ($P6$/mmm). An instructive description of this structure as a stacking of hexagonal planes with covalently bonded boron atoms that are separated by metal layers is given in figure 1(a). The boron atoms form graphite-like covalently bonded hexagons, with metal atoms above (and below) their centers. In addition to the predominant AlB_2 structure type, different structural modifications of diboride phases are known peculiar to late TMB_2 (such as WB_2, ReB_2, TaB_2, etc.). One such example is WB_2, for which different modifications are known. Recently, WB_2 thin films were reported to crystallize in the AlB_2 structure, whereas bulk material prefers the WB_2 modification, formerly known as W_2B_5. The WB_2 structure type is closely related to the AlB_2 prototype but it evidences a different layer structure, with both flat and puckered boron layers [16]. This results in an increased unit cell, containing twelve atoms and crystallizing in space group 194 ($P63$/mmc) as depicted in figure 1 (b).

Ternary transition metal borides are potential candidates as a coating for wear resistant applications when combining different structural modifications of TM-diborides (AlB_2- and WB_2-structured) which

---

*Corresponding author: shev@ipms.kiev.ua.
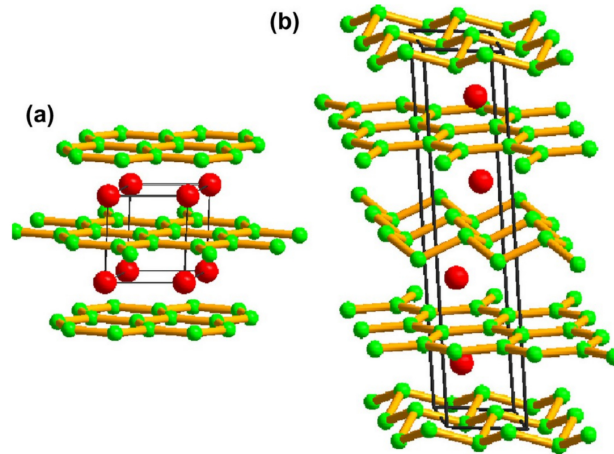
Figure 1. (Colour online) Unit cell and layer structure of (a) AlB_2 and (b) WB_2 prototypes [16].

exhibit good exploitation properties. However, while ternary transition metal nitrides and carbides as coatings were investigated in detail [17], ternary transition metal boride coatings are still much less explored. There is a limited amount of papers in which the ternary transition metal borides (M1,M2)B, where M1, M2 = La, Zr, W, Ti, Ta, Fe, Cr, Ni, Sc, Hf, V, Nb, Co, Mo, are studied.

On the other hand, first principles calculations of the structure and properties of such ternary borides are very important since the search of the optimum deposition parameters by means of trial and error method is not effective. A more promising approach is to combine experiment with calculations. Therefore, in our review we paid much attention to the calculations of the structure and mechanical properties of ternary boride systems. So far, there are no comprehensive review papers on the films based on ternary boride systems in which the first principles investigations could be reviewed together with experimental studies. Thus, in this paper we aimed at filling this gap in studying such a kind of films.

2. Theoretical studies

In combination with experimental research, the computational materials science creates an effective instrument for forecasting the structure and properties of materials. The structure and properties of some ternary transition metal borides were theoretically studied based on the first principle calculations within the framework of density functional theory (DFT).

As it was noted in Introduction section, the transition metal diborides can exist in two structural prototypes, namely: AlB_2 and WB_2. Despite the fact that the AlB_2 structure type is the predominant one, there also exist diboride phases which prefer to crystallize in other modifications. One such phase is WB_2, for which the two above mentioned structural modifications are reported. Due to the existence of the different structural modifications, combining AlB_2-structured TM-diborides with WB_2 ones can result in ternary systems that are based on combined allotropes. Euchner et al. [16] using DFT calculations investigated the supersaturated solid solution of ternary systems $Ti_xW_{1-x}B_2$ and $V_xW_{1-x}B_2$ with respect to structure formation and stability. To distinguish structural modifications, the symbols "a" and "w" were used to represent the AlB_2 (a-$M_xW_{1-x}B_2$) and the WB_2 prototypes (w-$M_xW_{1-x}B_2$), respectively.

Supersaturated solid solutions of a-$M_xW_{1-x}B_2$ are highly stable since they essentially show no tendencies for spinodal decomposition. When plotting the differences in energy of formation between a-$M_xW_{1-x}B_2$ and the isostructural constituent phases a-AlB_2 and a-WB_2, it becomes evident that the a-phase is stable against isostructural decomposition since ΔE_{mix} is negative (or very close to zero) for the whole composition range (cf. figure 2). This will be even further enhanced when configurational entropy is taken into account.

The fact that an interaction between two different allotropes may result in materials with improved physical properties is well known from the $Ti_{1-x}Al_xN$ system. These improvements in the physical
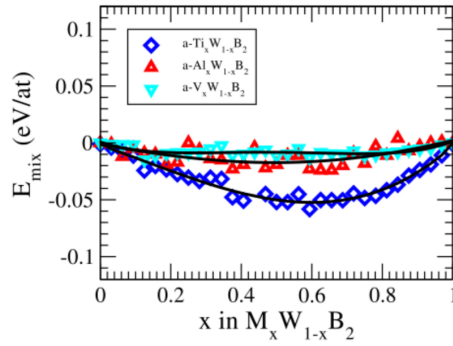
Figure 2. (Colour online) Enthalpy of mixing of $M_xW_{1-x}B_2$ with respect to the a-phase. The black curves are fits to the data [16].

properties originate from the interaction between the preference for hexagonal and cubic structure types of AlN and TiN. Following this idea of competing structure types, supersaturated solid solutions of ternary borides were studied, which are based on binary constituents that in principle prefer to crystallize in different modifications. It was shown on the exemplary cases of $Ti_xW_{1-x}B_2$ and $V_xW_{1-x}B_2$ that such ternary borides represent a new class of metastable materials which offer a large field for further investigations. The recent successful deposition of a-WB_2 together with the calculated formation energies allows the authors of [16] to conclude that solid solutions of a-$M_xW_{1-x}B_2$ type are experimentally accessible over a large composition range.

In [18], the crystal structures, mechanical properties and Debye temperatures of 18 transition metal ternary borides $M^I_xM^{II}B_x$ ($x = 1$ or 2, M^I and M^{II} are transition metals) were studied through first-principle calculations. The thermodynamic stability of the ternary borides crystal structures was estimated by the cohesive energy (E_{coh}) and formation enthalpy (ΔH_r). When both E_{coh} and ΔH_r are negative, the crystal structure is thermodynamically stable and the smaller the negative values are, the more stable the structure is.

The mechanical stability of the $M^I_xM^{II}B_x$ compounds was estimated using the criteria for elastic constants c_{ij}. The bulk modulus B, shear modulus G, Young's modulus E, and Poisson's ratio ν of the compounds were also determined. The ductility of a material can be evaluated by the B/G ratio and Poisson's ratio ν, namely, the larger the B/G and ν values are, the better is the ductility. Hardness is a key indicator for predicting the wear resistance of coating materials. Debye temperature is closely related to solid lattice vibration, thermal conductivity, thermal expansion and specific heat: solid materials with higher Debye temperatures tend to exhibit higher thermal conductivity.

The calculated Vickers hardness, Debye temperature, B/G ratio and Poisson's ratio are shown in figure 3. The main conclusions following from figure 3 are as follows: (1) the calculated formation enthalpy and respective elastic constants indicate that all the phases possess thermodynamic stability and mechanical stability; (2) the results of B/G values confirm that the $M^I_xM^{II}B_x$ ($x = 1$ or 2) except Ta_2FeB_2, Mo_2MnB_2, Nb_2CrB_2, Nb_2FeB_2 and Ti_2ReB_2, had a better ductility than the compound WC; besides, W_2MnB_2, Mo_2FeB_2, Mo_2NbB_2, Nb_2CrB_2, Nb_2FeB_2, Ti_2ReB_2, Mo_2CoB_2, Mo_2NiB_2, MoCoB and NbFeB show a larger Debye temperature than WC; (3) the predicted hardness of the $M^I_xM^{II}B_x$ ($x = 1$ or 2) ternary borides, based on the calculated overlap populations and Gao's hardness model, show that MoCoB exhibits the maximum hardness value of 26.3 GPa, which is still lower than that of WC; (4) by analyzing the density of states and Poisson's ratio ν, all the $M^I_xM^{II}B_x$ ($x = 1$ or 2) exhibit metallic, ionic and covalent hybrid properties; (5) according to the calculated results and phase diagrams, a high hardness and thermal conductivity of MoCoB-Co cermet consisting of hard phase MoCoB particles in a ductile Co matrix is proposed as a material with a particular promise for replacing WC in some applications. Obviously, all the hardness values of $M^I_xM^{II}B_x$ ($x = 1$ or 2) are less than the hardness of tungsten carbide (27–33.3 GPa), which means that there is still a certain difference between the ternary boride and the tungsten carbide considering only the hardness of the hard phase. However, these gaps are not large. In fact, the hardness of a material is not only affected by the intrinsic factors such as chemical composition and the underlying arrangement of atoms, but also by the extrinsic effects such as surface
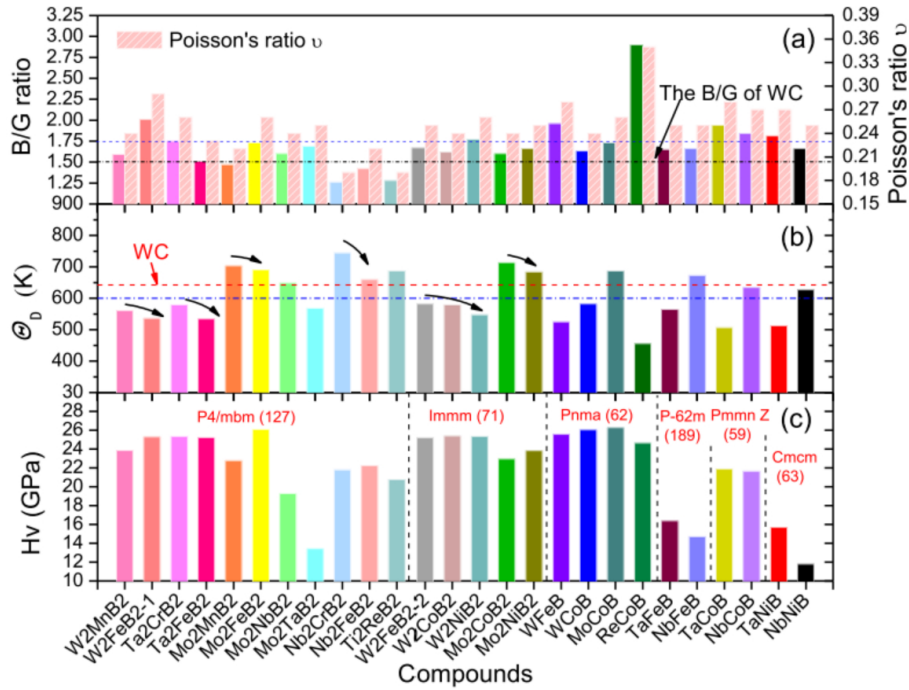
Figure 3. (Colour online) Some features of the $M_x^I M^{II} B_x$ ($x = 1$ or 2): (a) B/G ratio and Poisson's ratio v; (b) Debye temperature; (c) Hardness. For interpretation of the references to colour in this figure legend, the reader is referred to the Web version of this article [18].

morphology and grain structure of the material.

The results obtained also showed that the E_{coh} and ΔH_r of all the ternary transition metal borides are negative, indicating that the structures are stable. All the calculated elastic constants c_{ij} indicated a structural stability of the ternary borides considered. The ternary transition metal borides studied exhibited the hardness in the range of ~12 GPa (NbNiB) to ~26 GPa (MoCoB), high ductility and metallic, ionic and covalent hybrid properties.

Alling et al. [19] carried out investigations by first-principles using the density functional theory of the mixing thermodynamics of the alloy systems formed by $M_{1-x}^I M_x^{II} B_x$ combinations of the diborides ScB_2, YB_2, TiB_2, ZrB_2, HfB_2, VB_2, and TaB_2, all reported to crystallize in the AlB_2 type structure.

It is well known that lattice-matched systems can display clustering. Such alloys, with a small lattice mismatch, but a strong driving force for clustering are of particular interest for age-hardening potential. They are likely to form fully coherent interfaces and display spinodal decomposition with large composition fluctuations even when diffusion is limited. The resulting nanostructure in the lattice can decrease dislocation mobility and increase hardness. For this reason, the alloys $Al_{1-x}Ti_xB_2$, $Al_{1-x}V_xB_2$, $Mg_{1-x}Hf_xB_2$ deserve further attention because they are predicted to display clustering and a small volume misfit. Figure 4 shows the mixing enthalpies of ordered and disordered alloys for these systems, as well as for the ordering $Sc_{1-x}V_xB_2$ system for comparison.

The random TiB_2-ZrB_2 solid solutions were investigated in [20] by using the first-principles calculation. The results predict a positive deviation from Vegard's law for both the a and c parameters (cf. figure 5a). The positive curvature of the composition dependences of the lattice parameters may point to the instability of $Ti_{1-x}Zr_xB_2$. Indeed, the mixing energy for all compositions is positive (cf. figure 5), which indicates that the solid solution is not stable and will decompose into TiB_2 and ZrB_2 with the chemical driving force $\Delta E(x)$.

The phase diagrams of the TiB_2-ZrB_2 system, i. e., the concentration dependence of the decomposition temperature of the solid solutions according to the spinodal and binodal mechanisms, shown in figure 6, were computed with and without the contribution to the Gibbs free energy coming from vibration spectra (F_{Vib}) [20]. For both the spinodal and bimodal curves calculated without F_{Vib}, the maximum
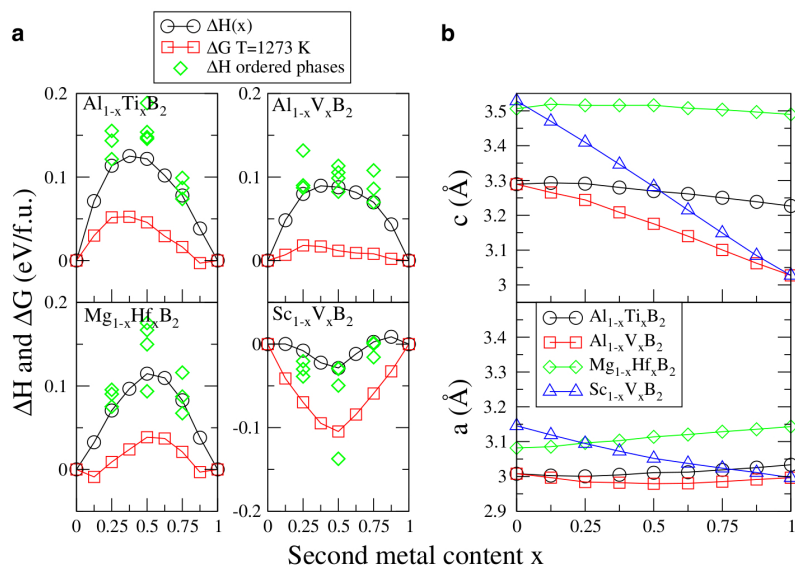
Figure 4. (Colour online) a) Mixing enthalpies of disordered and ordered alloys, as well as the mean field free energy at 1000°C for alloys that are identified as lattice matched clustering candidates, and an example of an ordering system, and b) c- and a-lattice parameters as a function of composition [19].
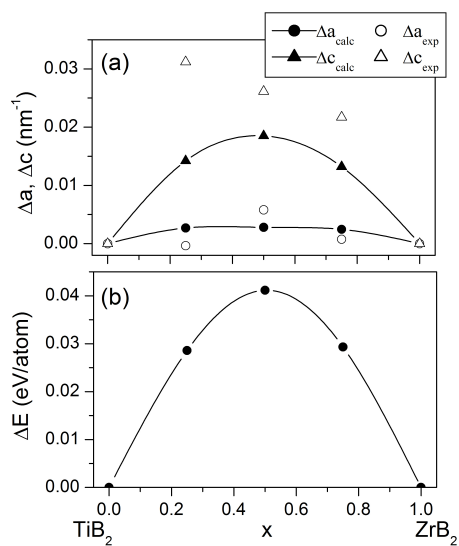
Figure 5. Deviation from linearity of the lattice parameters Δa and Δb (a) and mixing energy ΔE (b) for $Ti_{1-x}Zr_xB_2$. The calculated and experimental dependences are denoted by solid and dashed lines, respectively. Here, the lines are polynomial fits to the data points (to be considered as a guide to the eyes) [20].

decomposition temperature (consolute temperature, T_C) is 2418 K and the consolute composition (x_C) is 0.47. For the curves computed with contribution from F_{Vib}, T_C = 1973 K and x_C = 0.4. Therefore, it reduces the consolute temperature and shifts both the spinodal and binodal curves towards the TiB_2 (smaller-cation) side.
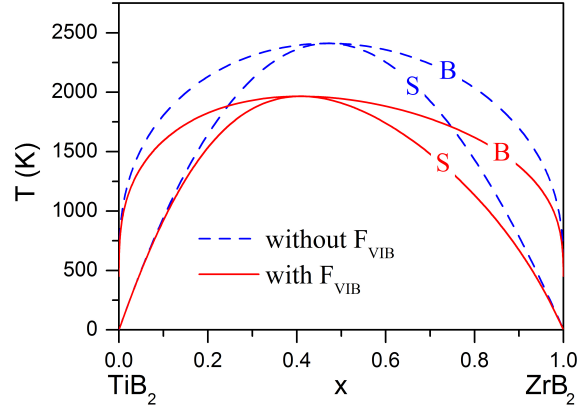

Figure 6. (Colour online) The calculated spinodal (S) and bimodal (B) curves for the $Ti_{1-x}Zr_xB_2$ alloys. Dashed blue curves are for calculations that did not include F_{Vib}, and solid red curves are for calculations that did [20].

The calculated Hill elastic moduli (B, G, E), Debye temperature (Q_D), Vickers hardness (H_V), B/G ratio and fracture toughness (K_{IC}) of the TiB_2-ZrB_2 alloys are shown in figure 7 as functions of composition [20]. A negative deviation of all the calculated characteristics from the mixing rule is observed. Poisson's ratio changes are in antiphase to the composition dependences of the elastic moduli G and E (not shown here). No strength enhancement was revealed: the hardness of the alloys does not exceed H_V of TiB_2 since the $H_V(x)$ dependence has a negative deviation from linearity. The fracture toughness for TiB_2 (3.74 MPa m$^{1/2}$) and ZrB_2 (3.45 MPa m$^{1/2}$) is in a rather good agreement with the experimental values. For TiB_2, the calculation slightly underestimates the experimental values of K_{IC}. The B/G ratio for TiB_2 and ZrB_2 was found to be 0.97 and 1.03, respectively, and this ratio for the alloys did not exceed these values (cf. figure 7e) indicating that the solid solutions should exhibit a brittle behavior.

In [23], the calculated total energy, electronic and phonon densities of states, elastic constants, hardness, shear and tensile ideal strengths, thermodynamic values for the random $Ti_{1-x}Nb_xB_2$ alloys were analyzed as functions of compositions. The calculated mixing energy (E_{mix}) of both Ti-Nb and Ti-Nb-B solid solutions (alloys) shown in figure [8] indicate that it is energetically favorable for Nb and Ti, as well as for NbB_2 and TiB_2 to mix and form the stable alloys, in agreement with experiment [24]. The minimum of the $E_{mix}(x)$ dependence falls on $x \approx 0.43$. It follows from figure [8] that the main contribution to the stabilization of the solid solutions comes from the direct Ti-Nb interactions, while the Ti-B-Nb correlations shift the mixing energy minimum towards the compositions enriched by titanium.

To clarify the role of the vibration spectra in the stabilization of the solid solutions, the phonon densities of states (PHDOS, $g(x)$) of $Ti_{1-x}Nb_xB_2$ and the composition weighted average PHDOSs of TiB_2 and NbB_2, $g_{av} = (1-x)g_{TiB_2} + xg_{NbB_2}$ were calculated and the results are shown in figure 9 [23]. For TiB_2, both the experimental and the calculated PHDOSs agree rather well. The difference between PHDOSs for $Ti_{1-x}Nb_xB_2$ ($g_{alloy}(x)$, solid line) and the composition weighted average PHDOSs of TiB_2 and NbB_2 ($g_{av}(x)$, dashed line) for each composition of the alloys takes place: $g_{av}(x)$ shifts towards larger x. However, the larger the PHDOS at large frequencies is, the larger (more positive) the contribution to the vibration free energy becomes. It follows that lattice vibrations will promote the stabilization of $Ti_{1-x}Nb_xB_2$ at finite temperatures.

The calculated elastic moduli, bulk-to-shear modulus ratio (B/G) and Vickers hardness for $Ti_{1-x}Nb_xB_2$ are shown in figure 10 as functions of composition. One can see that the calculated moduli for TiB_2 and NbB_2 agree well with those obtained in other experimental and theoretical studies. For the alloys, we see that the calculated bulk modulus increases, and the values of G, E and H_V decrease gradually
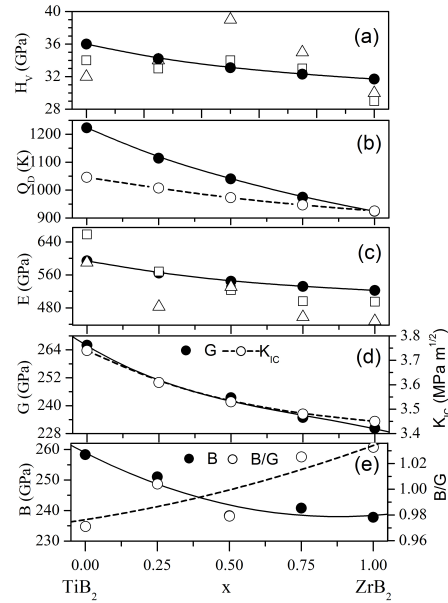
Figure 7. Vickers hardness (H_V), Debye temperature (Q_D) estimated using the elastic moduli (full circles) and the $C_V(T)$ dependences at T = 300 K (open circles), Hill Young (E), shear (G), bulk (B) moduli, facture toughness (K_{IC}) and B/G ratio of $Ti_{1-x}Zr_xB_2$ as functions of composition. Open triangles and squares are the experimental data from Refs. [21, 22], respectively [20].

with an increasing x. An extreme behavior of these values with composition was not observed: the solid solutions have always got lower values of the elastic constants and moduli than the composition weighted average values of TiB_2 and NbB_2, suggesting that the elastic properties are restricted by the individual components. To evaluate the alloying effect on the ductility, the ratio, B/G, as a function of concentration x is plotted in figure 10. The higher or lower the B/G ratio is, the more ductile or brittle the material is, respectively. The critical value that separates ductile and brittle materials is approximately 1.75. Figure 10 shows that the B/G ratio increases with x, although it does not reach the critical value. Based on the trends for the B/G ratio, one can conclude that the ductility of the alloys increases gradually as the Nb content increases.

In [26], the stability, electronic structures and mechanical properties of Mo_2FeB_2 and Mo_2NiB_2 ternary borides were investigated. Mo_2FeB_2 was found to display high hardness and strength as well as pretty good corrosion-resistance, which attracts much attention compared to other borides [27]. Mo_2NiB_2 was found to have two different structures with orthorhombic and tetragonal lattices (O-Mo_2NiB_2 and T-Mo_2NiB_2, respectively). Compared to Mo_2FeB_2, the Mo_2NiB_2 based cermets are supposed to show better high-temperature properties and corrosion resistance considering the existence of Ni. In this context, Mo_2NiB_2 is hypothetically more appropriate for the applications under the conditions of high temperature.

Shown in figure 11 are the calculated cohesive energy and formation enthalpy of three ternary borides. It can be seen that the cohesive energy and formation enthalpy are negative indicating that all the three borides are thermodynamically stable.

It can be found from figure 12a that the hardness shows a good consistence to the shear modulus of the three ternary borides. Young's modulus is defined as the ratio of stress to strain, which can reflect the stiffness of the solid. In this case, it can be concluded that O-Mo_2NiB_2 shows the highest stiffness with Mo_2FeB_2 and T-Mo_2NiB_2 followed by sequence. Moreover, Young's modulus can respond to the covalent bonding character of the material. Higher Young's modulus indicates a stronger covalent bonding. Thus, O-Mo_2NiB_2 can be considered to have the strongest covalent bonding while Mo_2FeB_2 and T-Mo_2NiB_2 show a relatively weaker covalent bonding character. Furthermore, it can be found that the Vickers hardness to Young modulus (H/E) ratio of O-Mo_2NiB_2 is slightly higher than that of Mo_2FeB_2 and T-Mo_2NiB_2. Figure 12b shows the B/G ratio and Poisson's ratio of the three ternary borides studied.
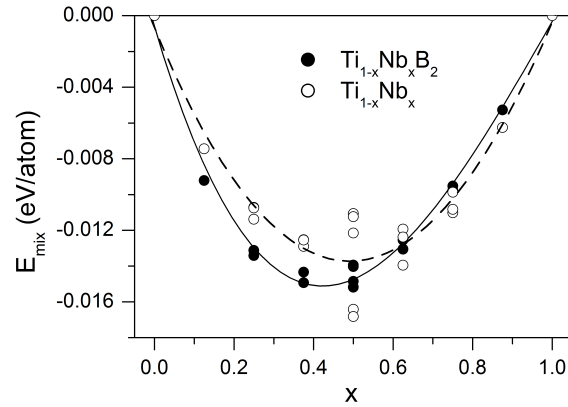
Figure 8. Energy of mixing versus composition for $Ti_{1-x}Nb_xB_2$ (solid circles and solid line) and hypothetical $Ti_{1-x}Nb_x$ (open circle and dashed line). The lines are the resulting polynomial fit to the calculated points [23].
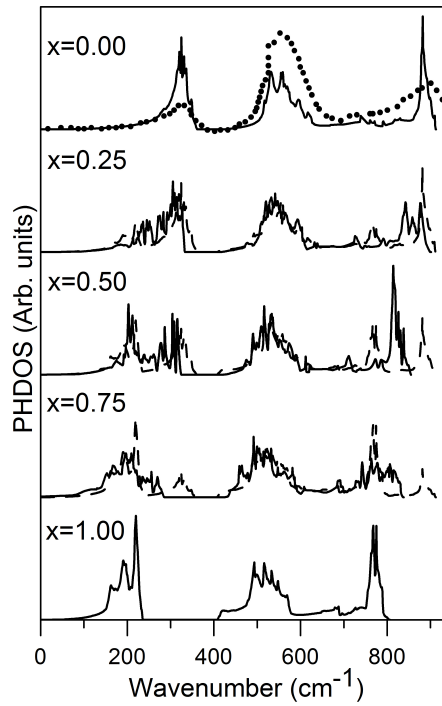
**Figure 9.** The calculated phonon density of states (PHDOS) for $Ti_{1-x}Nb_xB_2$ (solid line) and the composition weighted average PHDOSs of TiB_2 and NbB_2, $g_{av} = (1-x)g_{TiB_2} + xg_{NbB_2}$ (dashed line) [23]. For comparison, the experimental PHDOS measured using the technique of inelastic neutron scattering for TiB_2 is also presented (dotted line) [25].
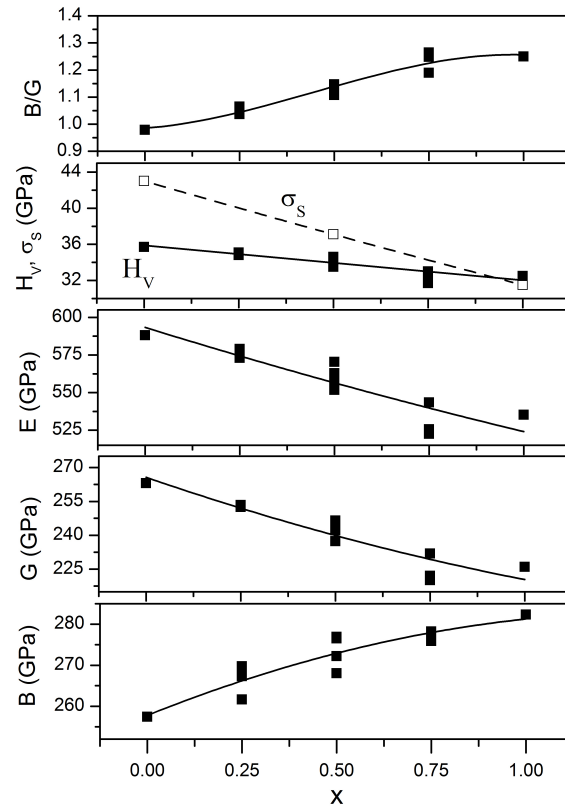
Figure 10. The calculated bulk modulus (B), elastic constants (G, E), Vickers hardness (H_V), ideal shear strength (σ_s), and B/G ratio for $Ti_{1-x}Nb_xB_2$ alloys as functions of concentration x (squares). The solid lines are the resulting cubic interpolation of the calculated points [23].
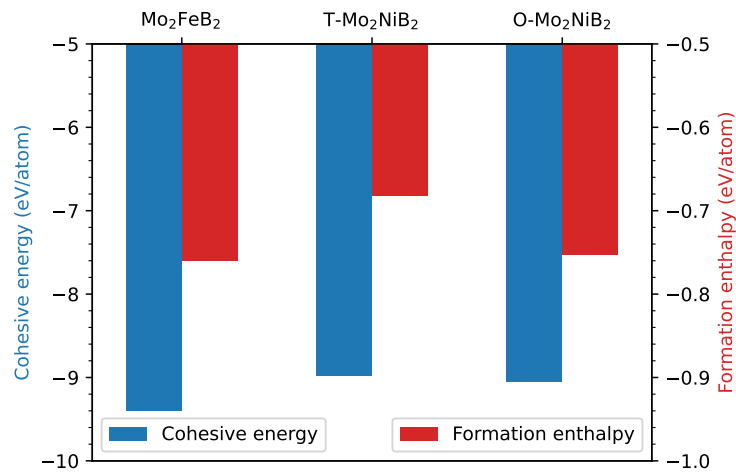
Figure 11. (Colour online) Cohesive energy and formation enthalpy of three ternary borides: Mo_2FeB_2, T-Mo_2NiB_2, O-Mo_2NiB_2 [26].

Generally, B/G ratio can be used to indicate the ductility of the material. It can be found that O-Mo_2NiB_2 exhibits the smallest B/G ratio, implying the weakest ductility. By comparison, T-Mo_2NiB_2 shows the best ductility with the B/G ratio of 1.923. Usually, the material possessing such high B/G can be classified as a ductile compound. As mentioned above, O-Mo_2NiB_2 has a strong tendency to covalent
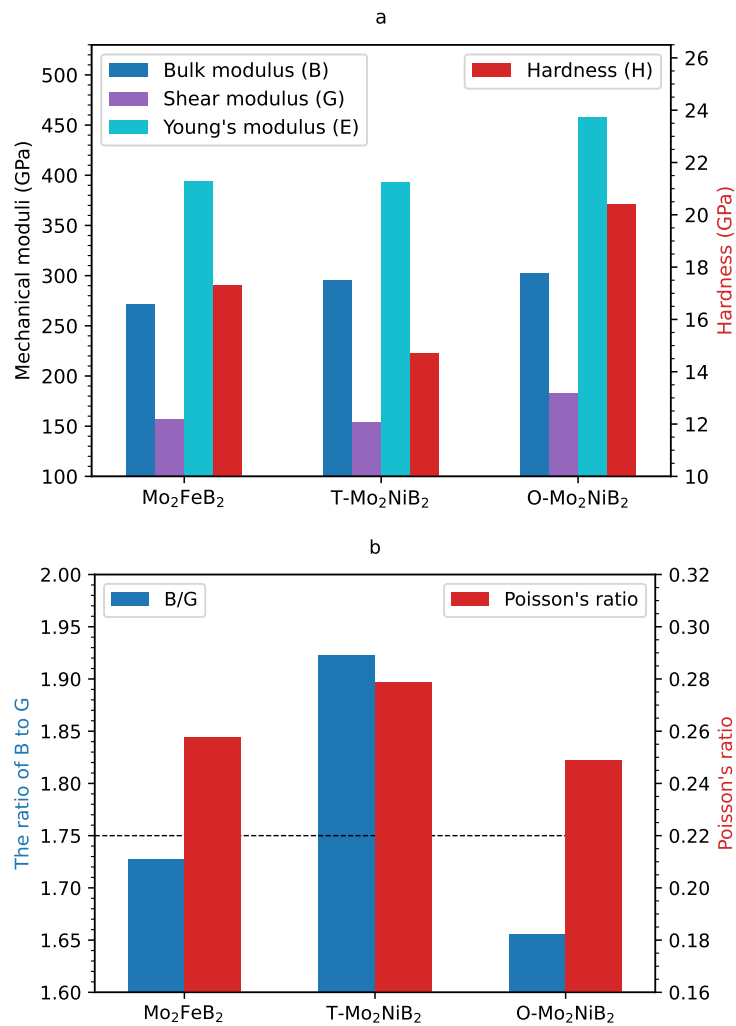
Figure 12. (Colour online) Mechanical properties of three ternary borides: (a) Moduli and Vickers hardness, (b) the ratio of B/G and Poisson's ratio [26].

bonding, which may be the main factor for its brittleness. On the contrary T-Mo_2NiB_2 shows a stronger tendency to metallic character, which is attributed to the typical tetragonal crystal structure.

Thus, the main results of the investigations of Mo_2FeB_2 and Mo_2NiB_2 ternary borides can be summarized as follows: (1) Mo_2FeB_2, T-Mo_2NiB_2 and O-Mo_2NiB_2 are all thermodynamically and mechanically stable, and O-Mo_2NiB_2 shows a better stability than T-Mo_2NiB_2. (2) O-Mo_2NiB_2 shows the highest Young's modulus and hardness such as 457.3 and 20.4 GPa, respectively; T-Mo_2NiB_2 has a comparable hardness and modulus to Mo_2FeB_2 while the ductility is obviously higher. (3) O-Mo_2NiB_2 shows the best isotropy among the three studied borides though it shows the strongest covalent bonding character.

3. Methods for deposition of ternary transition metal boride films/coatings

The main properties of condensates depend not only on their structure and chemical bonds, but also, to a great extent indirectly, on the deposition process itself. The films/coatings of transition metal ternary

borides were deposited using various techniques. The most commonly used technique for depositing ternary transition boride films is magnetron sputtering in which either one target prepared from mixture of respective elemental or binary boride powders [28–30], or co-deposition of two targets each prepared only by one of the binary borides which are constituents of the deposited film [31–37] are used. In the latter case, the units equipped with two magnetrons are suitable for the "dual" deposition process (figure 13).

In [38], the Fe-Cr-B coatings were deposited by detonation-gun thermal spraying method of powders of Fe-Cr-B alloy. The acetylene (C_2H_2) and oxygen (O_2) were used as fuel gases. In [39], the Ni-Cr-B coatings were prepared by this method through spraying NiCrB cored wires prepared by filling NiCr alloy tubes with the mixture of NiB, Cr and Ni powders.

In [32], the films of W-Zr-B were deposited by hybrid RF magnetron and pulsed laser method. The sputtering gas was argon. In this case, the target made of W_2B_5 was sputtered by magnetron whereas the target made of ZrB_2 was sputtered by laser (figure 14). One more technique used for depositing the ternary transition metal boride films is the arc spraying method.

4. Structure

The structure and elemental and phase composition of ternary boride films were studied by X-ray diffraction (XRD), time of flight elastic recoil detection analysis (TOF-ERDA), scanning electron microscopy (SEM), energy-dispersive spectroscopy (EDS), wavelength-dispersive spectroscopy (WDS), electron-probe microanalysis (EPMA), transmission electron microscopy (TEM), selective area elec-
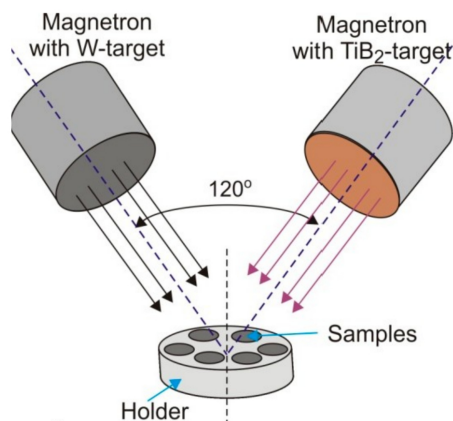

Figure 13. (Colour online) Scheme of the unit equipped with two magnetrons [31].
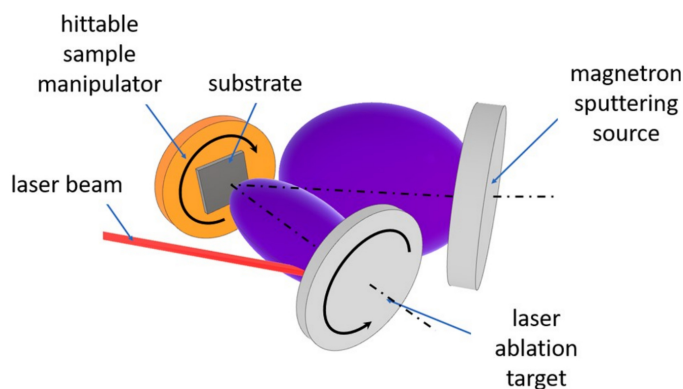
Figure 14. (Colour online) Scheme of magnetron sputtering combined with pulsed laser deposition [32].

tron diffraction (SAED), X-ray photoelectron spectroscopy (XPS), elastic recoil detection (ERD) and Rutherford backscattering (RBS), electron energy-loss spectroscopy (EELS).

The films in Ti-W-B system with different C_{Ti}-to-C_W ratio were studied in [28, 29, 31, 33]. In [33], the effect of tungsten addition on the microstructure and properties of the $Ti_xW_{1-x}B_2$ thin films was studied. Shown in figure 15 are typical XRD patterns of the $Ti_xW_{1-x}B_2$ thin films deposited on Si substrates [33]. XRD results show that all films are single phased and have crystallized — even at high tungsten content — in the AlB_2 structure type. With increasing tungsten content, both the (001) and the (011) reflections shift toward higher diffraction angles, whereas the (010) reflection remains at the position obtained for TiB_2. This indicates that replacing Ti by W results in the formation of $(Ti,W)B_2$ solid solution. Note that the content of Ti in the films studied was 12.8÷28.3 at. %. The shift of base reflections toward higher or lower diffraction angles was observed also in W-Zr-B [32], W-Ti-B [28, 29] and Zr-Ta-B [36] films. The shift of XRD reflections toward higher or lower diffraction angles depends on whether the adding atoms have larger or smaller radius compared to the base atoms. In these cases, the introduced atoms replace the base atoms and cause an increase or decrease of the unit cell (i. e., lattice parameter) due to compressive or tensile stress, and as a result we observe a shift of diffraction peaks.
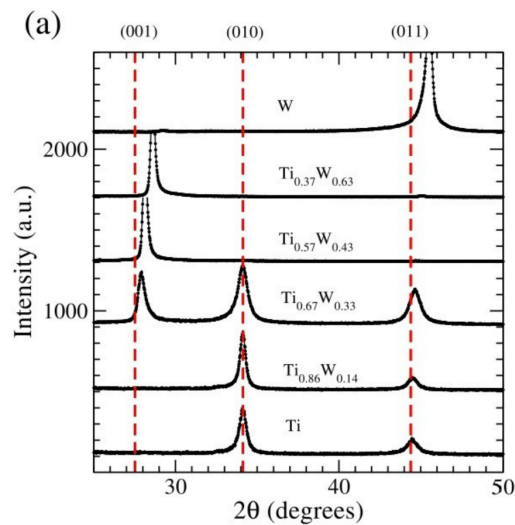
Figure 15. (Colour online) Diffraction patterns (grazing incidence) of $Ti_xW_{1-x}B_2$ thin films [33].

The Ti-W-B films with different content of Ti (0.6÷12.2 at. %) were also studied in [28]. It was revealed that at low Ti content (0.6 at. % $\leq$ Ti $\leq$ 4.6 at. %) there is formed a coherently bound nanocomposite β-(W,Ti)B/(Ti,W)B$_2$. At a content of 10.2 at. % Ti, the structure of the coating is ordered on the basis of $(Ti,W)B_2$ phase. XRD pattern also showed that with an increasing Ti content, the (101) $(Ti,W)B_2$ diffraction peak became relatively more intense. This indicated the presence of a preferred orientation of the grains in the films. The average crystallite size of the β-(W,Ti)B phase decreased in the interval $C_{Ti}/C_W < 0.15$. The observed change in the size of the crystallites is explained by the formation of the β-(W,Ti)B solid solution. When the content of titanium in the film is high, the size of the β-(W,Ti)B crystallites increases proportional to the ratio C_{Ti}/C_W. A linear increase in the lattice parameter with an increase in concentration of Ta in W-Ta-B films (figure 16) was observed in [30] with an excellent agreement to Vegard's relationship for substitutional solid solutions [40]. The formation of solid solution single-phase AlB_2-type TM boride films through partial replacing of the matrix TM atoms by the added TM atoms was also observed in W-Zr-B [32], W-Ti-B [32], W-Ta-B [30, 34], Fe-Cr-B [38], Ti-Ta-B [35], Zr-Ta-B [36], and Ni-Cr-B [39] ternary borides.

The structure of Ti-W-B films was also studied using SEM and TEM methods [28, 29, 31, 33]. Formation of an oriented grain structure in those films was observed. For instance, in [28] high-resolution SEM images of the cross-sectional area of Ti-W-B films showed that for a small content of titanium atoms in films, an unoriented structure is mainly formed (figure 17a). At a large content of Ti ($C_{Ti} \approx 10.2$ at. %),
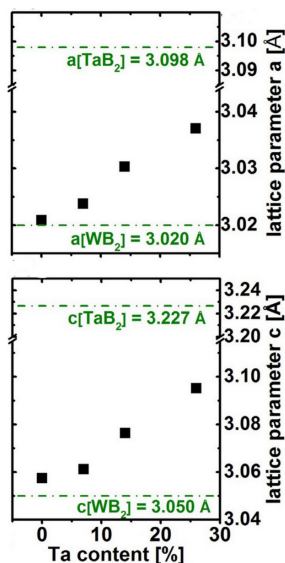
Figure 16. (Colour online) Lattice parameters (*a* and *c*) of the single-phased coatings (annealed at T_a = 800°C for 16 h in vacuum to ensure stress free states) vs. Ta content [30].

a columnar growth of crystallites occurred in the films (figure 17b). The high resolution TEM images of those films are shown in figure 18. As can be seen from the figure, in this case an ordered structure is formed (the average size of the ordering regions is about 10 nm). Formation of an oriented grain structure was also observed in W-Zr-B [32], W-Ta-B [30], Zr-Ta-B [36] and La-Zr-B [37] films.
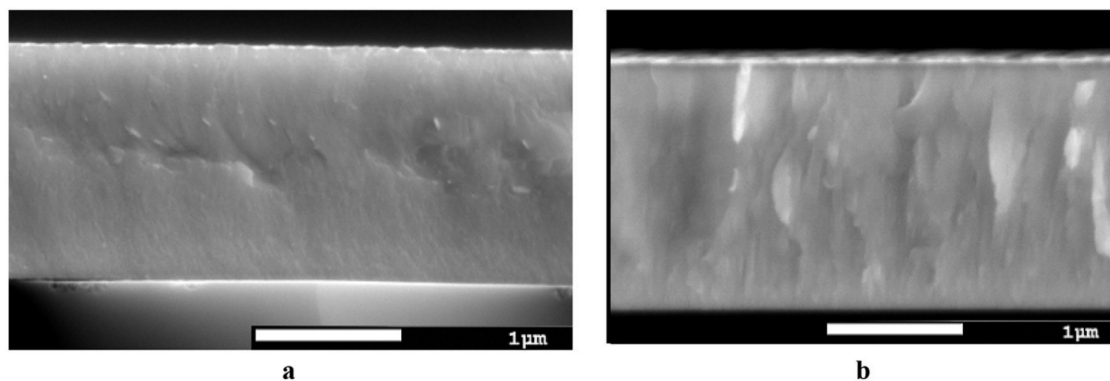
Figure 17. Cross-section SEM images of W-Ti-B films with content Ti, at. %: a — 1.9, b — 10.2 [28].

The XPS method was used to study the chemical bonds in ternary TM borides. In [32], the state of W, Zr and B bonds in the W-Zr-B films was investigated. It was revealed that only W-B and Zr-B bonds are presented in films with different content of zirconium, which is peculiar to W_2B_5 and ZrB_2 phases. No W-Zr bonds were found indicating the formation of solid solution as a result of replacing the tungsten atoms by zirconium atoms in the W-Zr-B lattice. Similar results were also obtained in W-Ti-B [29], Ta-W-B [34] and Zr-Ta-B [36] ternary TM boride films. On the whole, the results of XRD, ED, and XPS studies and the data on lattice parameter measurements allow us to make a conclusion that substitution solid solutions are formed in ternary transition metal borides.
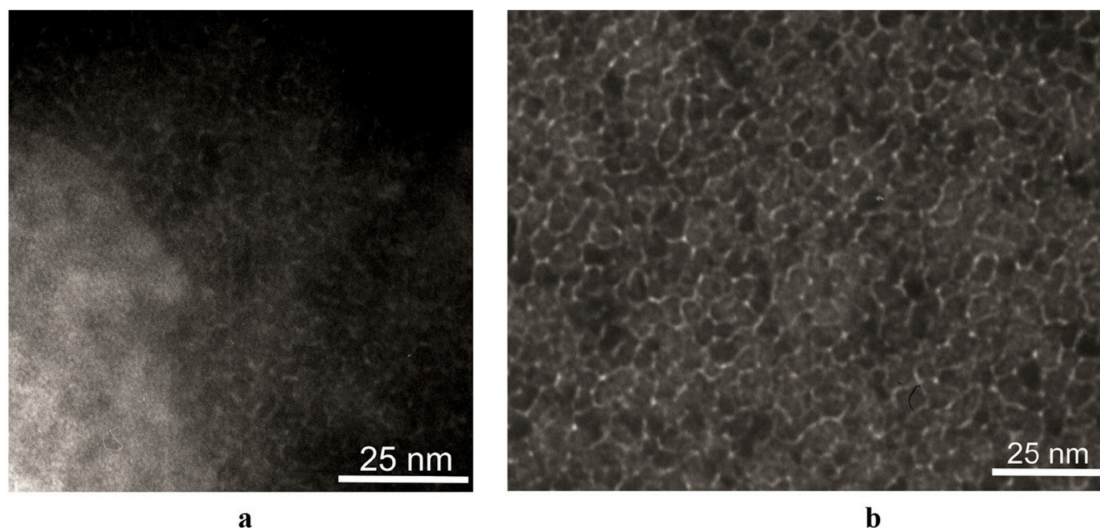
Figure 18. HR TEM images of W-Ti-B film with content Ti, at. %: a — 1.9, b — 10.2 [28].

5. Mechanical properties

Hardness and Young's modulus   The hardness of ternary transition metal borides was studied by various techniques (nanoindentation and microindentation) in films deposited onto different substrates (silicon single crystals, high-speed and stainless steels, polycrystalline Al_2O_3, single crystalline sapphire). Thus, the absolute values of the measured hardness and Young's modulus are different depending on the film-substrate-method combination. However, the analysis of publications showed that there are general tendencies to a change in the mechanical properties in ternary transition metal film borides.

The mechanical properties of the films in the Ti-W-B system were studied in [28, 29, 31, 33]. In [31], the effect of W addition on the hardness and Young's modulus of TiB_2 films was studied. The results obtained showed that those quantities steadily increased with addition of tungsten in amounts of 3-to-10 at. % due to the changes in the microstructure of coatings from a typical columnar structure of TiB_2 to a clear nano-composite structure of Ti-B-W (10 at. %). Similar dependence for Young's modulus of Ti-W-B films, as determined from nanoindentation, was observed in [33] with increasing W content in the range of 4.5-34.6 at. %. However, a pronounced maximum of the hardness was reached for W contents of 33 at. % and 43 at.% on the metal sublattice. Using ab initio methods, there were presented vacancies as a possible explanation for the stabilization of the α-phase in this ternary system.

The effect of Ti content on the hardness and Young's modulus of W-Ti-B films was studied in [28, 29]. Sobol et al. [28] showed that these quantities steadily increase with increasing Ti concentration from 0.6 at. % to 10.2 at. % as a result of coating structure to become ordered on the basis of $(Ti,W)B_2$ phase. Quite different result was obtained by Moscicki et al. [29]. They showed that the deposited films without titanium exhibit properties as presented in literature, namely: due to the crystalline columnar structure, hardness reached 49.0±0.6 GPa with effective elastic modulus of 709.4±89.5 GPa (figure 19). Addition of 2 at. % Ti caused a two-fold decrease of the hardness and elastic modulus. This was a result of changing highly oriented crystalline structure to amorphous phase. The increasing of titanium content to $C_{Ti} \approx$ 3.6 at. % caused about 20 % rise of the hardness and effective elastic modulus to 37.5±1.9 GPa and 341.2±2.4 GPa, respectively. The highest hardness and elastic modulus values were measured for $C_{Ti} \approx$ 5.5 at. %. The observed variation of these quantities was explained by structural changes in the films first from crystalline to amorphous phase and next to hexagonal α-$(W,Ti)B_2$ structure at a higher content of titanium.

Similar behavior of the hardness and elastic modulus was observed in W-Zr-B films [32]. With increasing Zr content, the hardness and elastic modulus reduced slightly, and then increased up to maximum values. The decrease in mechanical properties of films with addition of Zr was explained
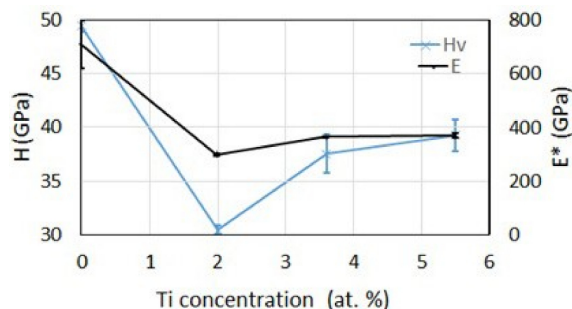
Figure 19. (Colour online) Hardness and effective elastic modulus of the deposited films as function of Ti concentration [29].

by structural changes in films. At a low Ti content, an amorphization and, as a result, a decrease in compressive stress occurred. At higher Zr contents, the crystallization of a film resulted in the formation of nanocomposite in which crystals of ZrB_2 are imbedded in the Ti-Zr-B matrix. The alloying of WB_2 with zirconium also allows to change the elastic properties from brittle to ductile while maintaining the film superhardness and incompressibility [32].

In [35], the hardness and elastic modulus of Ti-Ta-B films were investigated. The variation of tantalum content in the films was attained by increasing the sputtering current at the TaB_2 target. By increasing the TaB_2 target current, a slight increase in hardness and elastic modulus was observed up to stoichiometric $Ti_{0.18}Ta_{0.81}B_2$ coating. By further increase of TaB_2 target current, a decrease of both mechanical properties took place (figure 20). The observed variations of hardness and elastic modulus were attributed to the structure and stress measured in the deposited films. It was shown that at low Ta content, the film structure exhibited a columnar nature and enhanced the compressive macrostress. The decrease of compressive macrostress in understoichiometric coatings (B/Me < 2 in figure 10) is related to the transition from textured nanocolumnar to amorphous structure.
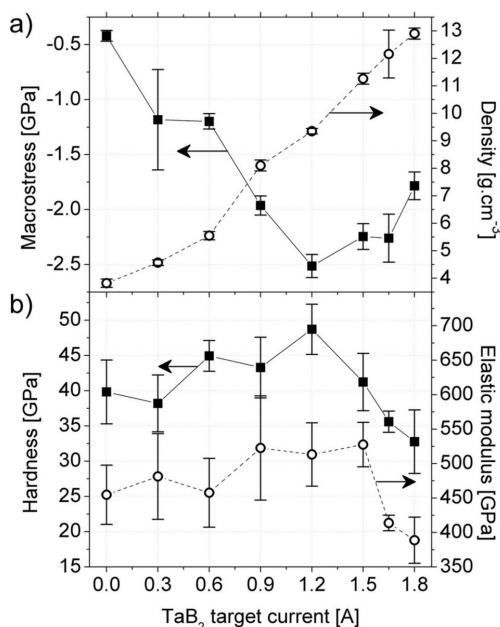
Figure 20. (a) Macrostress and density and (b) hardness and elastic modulus of co-deposited Ti-Ta-B films [35].

A similar dependence of hardness and elastic modulus on the content of alloying transition metal (Ta) was revealed for Zr-Ta-B films [36]. With addition of Ta, the hardness and elastic modulus increased up to

maximum values, and then decreased. The films with low content of Ta had a columnar structure in which thin B-rich tissue phase, with strong covalent bonding, located at the column boundaries which inhibits a column-boundary sliding. An increase in mechanical properties was also attributed to the solid-solution hardening effect. The author of [36] also observed a decrease in the column width with addition of Ta that also adds hardness to the film via the Hall-Petch effect. A further increase in Ta content resulted in the structure transformation towards amorphous-like phase with grain boundaries enriched with metallic Ta, which results in a decrease of hardness and elastic modulus of Zr-Ta-B films.

Strength properties The fracture toughness of transition metal borides was studied in [31, 35, 36] using nanoindentation technique. In [31], the resistance to brittle cracking of Ti-W-B films was investigated. The analysis carried out according to the Laugier model showed that, as a result of doping the TiB_2 coating with tungsten, there is a significant increase in its fracture toughness. For concentrations of 3-6 at.% W, the fracture toughness of Ti-B-W coatings reaches the value comparable to K_{IC} suitable for TiN and CrN coatings. The fracture toughness of Ti-B-W with 10 at. % W is $K_{IC} = 4.98$ MPa·m$^{1/2}$ and is nearly 7.5 times higher than for the TiB_2 coating ($K_{IC} = 0.67$ MPa·m$^{1/2}$).

Grančič et al. [35] studied the fracture toughness of Ti-Ta-B films. It was shown that the coating structure and B/Me ratio appears to have an important effect on the toughness of coatings. The coatings with B/Me > 2 exhibited a nanocolumnar structure and revealed a lower toughness. The under-stoichiometric (B/Me < 2) coatings with amorphous or nearly amorphous structure showed an increased toughness.

Fracture toughness of Zr-Ta-B films was studied in [36]. It was revealed that with addition of Ta in Zr-B films, the toughness increased from $K_{IC} = 4.0$ MPa·m$^{1/2}$ for $ZrB_{2.4}$ to 4.6 MPa·m$^{1/2}$ and 5.2 MPa·m$^{1/2}$ for $Zr_{0.8}Ta_{0.2}B_{1.8}$ and $Zr_{0.7}Ta_{0.3}B_{1.5}$ film compositions, respectively. The nanostructures of these alloys consisted of a hard columnar phase with metal-rich boundaries which inhibited the crack propagation while allowing grain-boundary sliding under heavy loads. Thus, $Zr_{0.8}Ta_{0.2}B_{1.8}$ and $Zr_{0.7}Ta_{0.3}B_{1.5}$ films exhibited a dual hard/tough nature: the tough metal-rich phase at the boundaries accommodates the ductility while the stiff nanosized columns provide high hardness.

Tribology Wear resistance substantially depends on the properties that are inherent in the films, namely: morphology, hardness, coefficient of friction, and cohesion [41]. The state of stress in the films is also important. In this regard, compressive residual stresses are preferred, since tensile stress is contributes to the cracking of the films under load.

Moscicki et al. [29] studied the wear resistance of W-Ti-B films. The comparative tribological test was conducted for of the W-B and W-Ti (5.5 at. %)-B coatings. The coating with titanium addition exhibited a higher wear resistance which resulted from the structure of the compared layers. Due to its compact structure, the titanium-alloyed film had a lower hardness, although the crack resistance was higher. The non-columnar structure contained fewer defects, which made the film more ductile and resistant to cracking. The friction coefficient was lower for the W-Ti-B film than for the W-B film (figure 21).
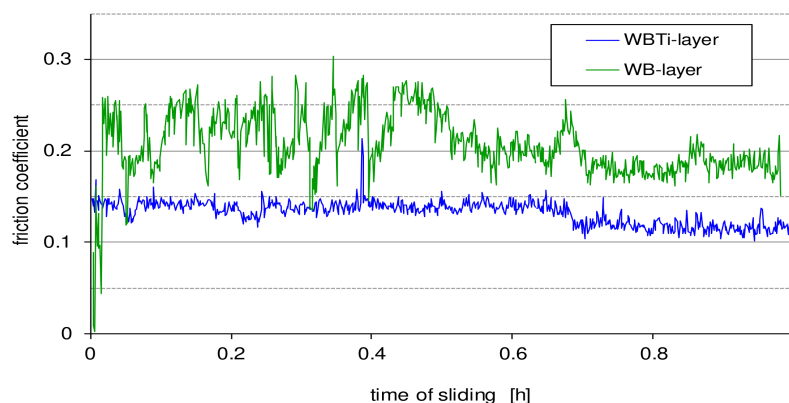

Figure 21. (Colour online) The time-dependent behavior of the friction coefficient of W-Ti(5.5 at. %)-B and W-B coatings [29].

Thermal stability   Euchner et al. [33] studied the effect of annealing on the structure and properties of W-doped (4.5 to 34.6 at. % W) TiB$_2$ films. They showed that these films exhibited no changes in their XRD patterns upon 30-min vacuum annealing at 1000℃ suggesting an outstanding thermal stability of a dense growth morphology. A similar result was obtained in a vacuum annealed W-Ta(7–26 at. %)-B films [30]. All compositions remained in their single-phased α-structure up to 800℃. At 1000℃, the binary metastable α-WB$_{2-z}$ decomposed to form t-WB and ω-W$_2$B$_{5-z}$. The addition of just 7 at. % Ta to the metal sublattice postponed the decomposition and transformation of the α-structure to 1200℃. Further alloying of Ta even increased the decomposition temperature and ensured the thin film materials for Ta contents above 14 at. % to be single-phased α-structured even up to 1200℃. These results prove the concept of stabilizing phases due to the addition of an appropriate alloying element.

Oxidation and corrosion resistance   Oxidation behavior in the ambient air of Ta-W-B films was investigated in [34]. The compositions in the full range from WB$_{2-z}$, W$_{0.85}$Ta$_{0.15}$B$_{2-z}$, W$_{0.66}$Ta$_{0.34}$B$_{2-z}$, W$_{0.42}$Ta$_{0.58}$B$_{2-z}$, W$_{0.19}$Ta$_{0.81}$B$_{2-z}$, to TaB$_{2-z}$ were studied. The oxidation tests in the ambient air at 500, 600, 700℃ for 1, 10, 100 and 1000 min showed a decrease in the oxide layer thickness with increasing Ta content for all temperatures applied (figure 22). Generally, the addition of Ta to WB$_{2-z}$ based coatings retarded the oxide scale kinetics through the formation of denser, less volatile, and adherent scales, which is a key factor for the enhanced oxidation resistance. An optimum composition of W$_{1-x}$Ta$_x$B$_{2-z}$ coatings would be in the range of $x = 0.2 - 0.3$, combining the enhanced fracture toughness ($\geqslant 3.0$ MPa·m$^{1/2}$) and the super hardness ($\geqslant 40$ GPa) next to a decent oxidation resistance.
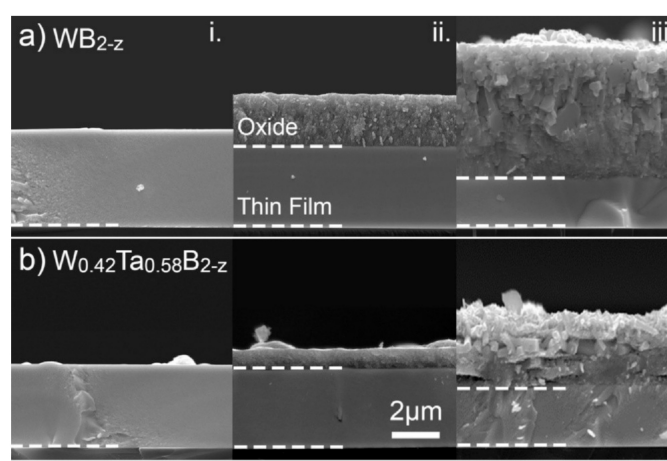
Figure 22. Cross sectional micrographs of (a) WB$_{2-z}$ and (b) W$_{0.42}$Ta$_{0.58}$B$_{2-z}$ oxidized films. Sections (a), (b) show selected coatings in (i) as deposited state, (ii) after 100 min of oxidation at 600℃ and (iii) after 100 min of oxidation at 700℃. The dashed lines are highlighting the interface between substrate and film as well as between film and oxide scale (from bottom to top) [34].

Corrosion resistance of W-Ti-B films placed onto the plates of 304 stainless steels (SS 304) was investigated in the electrochemical corrosion tests — impedance spectroscopy and polarization — in 0.5M NaCl solution [29]. As it was shown by structure study, the addition of titanium to the WB$_2$ caused the Ti-doped films to become denser and to lose their columnar structure. As a result, less direct diffusion paths for the corrosive medium were formed which resulted in the improvement of corrosion resistance. The best protective efficiency was achieved for W$_{0.92}$Ti$_{0.08}$B$_{4.5}$ coating. The protective efficiency decreased with the rise of titanium content and the associated increase in hardness.

The effect of boron on the corrosion resistance of Ni-Cr-B coatings deposited on commercial steel SA213-T2 by spraying NiCrB cored wires was also investigated in the electrochemical corrosion tests [39]. The hot corrosion tests were performed at 800℃ in molten mixed salt Na$_2$SO$_4$ + 10 wt. % NaCl for 200h with duration of 10h to evaluate the corrosion behavior of the coatings. The results obtained showed that boron promoted a successive and thin protective oxide scale on the surface of NiCrB coatings. The coatings with B content 0.5–3 wt. % had a much lower weight gain in the hot corrosion test. However, too

much boron was harmful to hot corrosion property due to the brittle borides and stress-inducing cracks, which worked as the path tunnel of the corrosion substance.

Future prospects for research   The research of metal borides is a very old field, and ever since the structure and wide range of metal diborides have been studied exhaustively. Therefore, it is necessary to move to ternary and higher borides as starting materials. These compositions are all the more challenging due to the factors such as phase stability relative to metal substitutions and simultaneous equilibrium of several phases in the product. The vast array of determined crystal structures to date offers a potential for targeted approaches to the prediction of structure and properties.

Supersaturated solid solutions of many ternary borides have been studied here, which are based on binary constituents that in principle prefer to crystallize in the same or different structural modifications. It was shown that such ternary borides represent a new class of materials having useful properties. The results obtained for ternary borides open the prospects for developing new materials based on combination of metal diborides in quaternary structures or even high entropy alloys. The design of such alloys may not be so difficult if their approximate optimal composition is known. The latter is quite possible when the results of first principles calculations are available. Therefore, we foresee that the combination of experiment and first principles calculations should be a particularly successful approach in the development of the films based on complex high-entropy alloys.

6. Conclusions

The review of recent achievements in the bulk and film materials based on ternary transition metal diboride alloys is given. First principles investigations of the structure and properties of the $M_{1-x}^{I}M_x^{II}B_2$ and $M_x^{I}M^{II}B_x$ ($x = 1$ or 2, M^I and M^{II} are transition metals) ternary borides showed that they possess high hardness, and hence high fracture toughness and exhibit ductility comparable to the ductility of WC (except for $Ti_{1-x}Zr_xB_2$ alloys that are highly brittle materials). These characteristics and the capability of controlling the properties by changing the composition make the ternary boride alloys suitable for many applications. Among them is the use of these alloys as the main components in wear-resistant and protective coatings resistant to extremely high temperatures.

The ternary boride films based on transition metal diborides can form solid solution single-phase AlB_2-type or WB_2-type structures through partial replacing of the matrix atoms by the added atoms of another transition metal. The formation of solid solutions is experimentally accessible over a large composition range. The films exhibit a dense columnar or near-amorphous structure which is stable upon annealing up to 1200℃. Ternary transition metal borides show a fairly high level of hardness, fracture toughness, good tribological properties. Therefore, the films of ternary transition metal borides have good prospects as materials used as protective coatings in various fields of technology.

References

1. Magnuson M., Hultman L., Högberg H., Vacuum, 2022, **196**, 110567, doi:10.1016/j.vacuum.2021.110567.
2. Choi H. S., Park B., Lee J. J., Surf. Coat. Technol., 2007, **202**, No. 4–7, 982–986, doi:10.1016/j.surfcoat.2007.06.020.
3. Chrzanowska J., Kurpask Ł., Giżyński M., Hoffman J., Szymański Z., Moiścicki T., Ceram. Int., 2016, **42**, 12221–12230, doi:10.1016/j.ceramint.2016.04.166.
4. Fahrenholtz W. G., Hilmas G. E., Talmy I. G., Zaykoski J. A., J. Am. Ceram. Soc., 2007, **90**, 1347–1364, doi:10.1111/j.1551-2916.2007.01583.x.
5. Rahman M., Wang C. C., Chen W., Akbar S. A., Mroz C., J. Am. Ceram. Soc., 1995, **78**, 1380–1382, doi:10.1111/j.1151-2916.1995.tb08498.x.
6. Cui X., Wang J., Wen M., Dai X., Miao K., Wang K., Zhang K., Ceram. Int., 2020, **46**, 9854–9862, doi:10.1016/j.ceramint.2019.12.260.
7. Jayaraman S., Gerbi J. E., Yang Y., Kim D. Y., Chatterjee A., Bellon P., Girolami G. S., Chevalier J. P., Abelson J. R., Surf. Coat. Technol., 2006, **200**, 6629–6633, doi:10.1016/j.surfcoat.2005.11.040.

8. Malinovskis P., Palisaitis J., Persson P. O. Å., Lewin E., Jansson U., J. Vac. Sci. Technol., A, 2016, **34**, 031511, doi:10.1116/1.4948234.

9. Merriles D. M., Nielson C., Tieu E., Morse M. D., J. Phys. Chem. A, 2021, **125**, 4420–4434, doi:10.1021/acs.jpca.1c02886.

10. Nedfors N., Tengstrand O., Lu J., Eklund P., Persson P. O. Å., Hultman L., Jansson U., Surf. Coat. Technol., 2014, **257**, 95–300, doi:10.1016/j.surfcoat.2014.07.087.

11. Prakash B., Richter E., Pattyn H., Celis J. P., Surf. Coat. Technol., 2003, **173**, 50–160, doi:10.1016/S0257-8972(03)00518-8.

12. Randich E., Thin Solid Films, 1980, **72**, 517–522, doi:10.1016/0040-6090(80)90541-6.

13. Rau J. V., Latini A., Generosi A., Albertini V. R., Ferro D., Teghil R., Barinov S. M., Acta Mater., 2009, **57**, 673–681, doi:10.1016/j.actamat.2008.10.009.

14. Sen S., Surf. Coat. Technol., 2005, **190**, 1–6, doi:10.1016/j.surfcoat.2004.07.120.

15. Shappirio J. R., Finnegan J. J., Thin Solid Films, 1983, **107**, 81–87, doi:10.1016/0040-6090(83)90010-X.

16. Euchner H., Mayrhofer P. H., Thin Solid Films, 2015, **583**, 46–49, doi:10.1016/j.tsf.2015.03.035.

17. Onoprienko A. A., Ivashchenko V. I., J. Superhard Mater., 2021, **43**, 231–247, doi:10.3103/S1063457621040079.

18. Yang G., Yin H., Xu Z., Zhang T., Yang J., Gao F., Zheng Q., Qu X., J. Alloys Compd., 2019, **791**, 761–772, doi:10.1016/j.jallcom.2019.03.389.

19. Alling B., Högberg H., Armiento R., Rosen J., Hultman L., Sci. Rep., 2015, **5**, 9888, doi:10.1038/srep09888.

20. Ivashchenko V. I., Turchi P. E. A., Shevchenko V. I., Mediukh N. R., Gorb L., Leszczynski J., Mater. Chem. Phys., 2021, **263**, 124340, doi:10.1016/j.matchemphys.2021.124340.

21. Karthiselva N. S., Murty B. S., Srinivasa R. B., In: Developments in Strategic Materials and Computational Design, Kriven W. M., Zhu D., Moon K. I., Hwang T., Wang J., Lewinsohn C., Zhou Y. (Eds.), J. Am. Ceram. Soc., 2015, 275–285, doi:10.1002/9781118217542.

22. Karthiselva N. S., Srinivasa R. B., Technologies, 2016, **4**, 30, doi:10.3390/technologies4030030.

23. Mediukh N. R., Turchi P. E. A., Ivashchenko V. I., Shevchenko V. I., Comput. Mater. Sci., 2017, **129**, 82–88, doi:10.1016/j.commatsci.2016.11.053.

24. Lampman S., In: ASM Handbook. 10th Ed. Vol. 2. Properties & Selection Nonferrous Alloys & Special Purpose Materials, ASM International, 1990, 592–633, doi:10.31399/asm.hb.v02.a0001081.

25. Heid R., Renker B., Schober H., Adelmann P., Ernst D., Bohnen K.-P., Phys. Rev. B, 2003, **67**, 180510(R), doi:10.1103/PhysRevB.67.180510.

26. Jian Y., Huang Z., Liu X., Xing J., Results Phys., 2019, **15**, 102698, doi:10.1016/j.rinp.2019.102698.

27. Yang F., Wu Y., Han J., Meng J., J. Alloys Compd., 2016, **665**, 373–380, doi:10.1016/j.jallcom.2016.01.053.

28. Sobol O. V., Dub S. N., Pogrebnjak A. D., Mygushchenko R. P., Postelnyk A. A., Zvyagolsky A. V., Tolmachova G., Thin Solid Films, 2018, **662**, 137–144, doi:10.1016/j.tsf.2018.07.042.

29. Moscicki T., Psiuk R., Słomińska H., Levintant-Zayonts N., Garbiec D., Pisarek M., Bazarnik P., Nosewicz S., Chrzanowska-Giżyńska J., Surf. Coat. Technol., 2020, **390**, 125689, doi:10.1016/j.surfcoat.2020.125689.

30. Moraes V., Fuger C., Paneta V., Primetzhofer D., Polcik P., Bolvardi H., Arndt M., Riedl H., Mayrhofer P., Scr. Mater., 2018, **155**, 5–10, doi:10.1016/j.scriptamat.2018.06.005.

31. Smolik J., Kacprzynska-Gołacka J., Sowa S., Piasek A., Coatings, 2020, **10**, 807, doi:10.3390/coatings10090807.

32. Psiuk R., Milczarek M., Jenczyk P., Denis P., Jarząbek D., Bazarnik P., Pisarek M., Moscicki T., Appl. Surf. Sci., 2021, **570**, 151239, doi:10.1016/j.apsusc.2021.151239.

33. Euchner H., Mayrhofer P. H., Riedl H., Klimashin F. F., Limbeck A., Polcik P., Kolozsvari S., Acta Mater., 2015, **101**, 55–61, doi:10.1016/j.actamat.2015.08.048.

34. Fuger C., Schwartz B., Wojcik T., Moraes V., Weiss M., Limbeck A., Macauley C., Hunold O., Polcik P., Primetzhofer D., Felfer P., Mayrhofer P., Riedl H., J. Alloys Compd., 2021, **864**, 158121, doi:10.1016/j.jallcom.2020.158121.

35. Grančič B., Pleva M., Mikula M., Čaplovičová M., Satrapinskyy L., Roch T., Truchlý M., Sahul M., Gregor M., Švec P., Zahoran M., Kúš P., Surf. Coat. Technol., 2019, **367**, 341–348, doi:10.1016/j.surfcoat.2019.04.017.

36. Bakhit B., Engberg D. L. J., Lu J., Rosen J., Högberg H., Hultman L., Petrov I., Greene J. E., Greczynski G., J. Vac. Sci. Technol. A, 2019, **37**, 031506–12, doi:10.1116/1.5093170.

37. Mitterer C., Ott H.-M., Komenda-Stallmaier J., Schmölz P., Werner W., Störi H., J. Alloys Compd., 1996, **239**, 183–192, doi:10.1016/j.surfcoat.2019.03.058.

38. Jin H., Park C., Kim M., Surf. Coat. Technol., 1999, **113**, 103–112, doi:10.1016/S0257-8972(98)00829-9.

39. Wang X., He D., Guo X., Zhou Z., Wang G., Guo F., Surf. Coat. Technol., 2019, **367**, 173–178, doi:10.1016/j.surfcoat.2019.03.058.

40. Denton A. R., Ashcroft N. W., Phys. Rev. A, 1991, **43**, 3161–3164, doi:10.1103/PhysRevA.43.3161.

41. Chiba Y., Omura T., Ichimura H., J. Mater. Res., 1993, **8**, 1109–1115, doi:10.1557/JMR.1993.1109.

Структура та властивості плівок на основі боридів потрійних перехідних металів: теорія та експеримент

А. А. Онопрієнко, В. І. Іващенко, В. І. Шевченко

Інститут проблем матеріалознавства ім. І. М. Францевича НАН України, Київ, Україна

В огляді приведено результати теоретичних та експериментальних досліджень структури, зв'язку між атомами, механічних властивостей, термічної стабільності, стійкості до окислення та корозії плівок на основі боридів потрійних перехідних металів.

Ключові слова: *потрійні бориди перехідних металів, плівки, структура, властивості*